Electro-optic modulation of solution-processed molybdenum disulfide

Songwei Liu,[1] Yingyi Wen,[1] Jingfang Pei,[1] Xiaoyue Fan,[2] Yongheng Zhou,[3] Yang Liu,[1,4] Ling-Kiu Ng,[1] Yue Lin,[5] Teng Ma,[6] Panpan Zhang,[7] Xiaolong Chen,[3] Gang Wang,[2,*] and Guohua Hu[1,†]

[1] *Department of Electronic Engineering, The Chinese University of Hong Kong, Shatin, N. T., Hong Kong S. A. R., China*

[2] *Centre for Quantum Physics, Key Laboratory of Advanced Optoelectronic Quantum Architecture and Measurement (MOE), School of Physics, Beijing Institute of Technology, Beijing 100081, China*

[3] *Department of Electrical and Electronic Engineering, Southern University of Science and Technology, Shenzhen 518055, China*

[4] *Shun Hing Institute of Advanced Engineering, The Chinese University of Hong Kong, Shatin, N. T., Hong Kong S. A. R., China*

[5] *CAS Key Laboratory of Design and Assembly of Functional Nanostructures, and State Key Laboratory of Structural Chemistry, Fujian Institute of Research on the Structure of Matter, Chinese Academy of Sciences, Fuzhou, Fujian 350002, China*

[6] *Department of Applied Physics, Hong Kong Polytechnic University, Hung Hom, Kowloon, Hong Kong S. A. R., China*

[7] *State Key Laboratory of Information Photonics and Optical Communications, Beijing University of Posts and Telecommunications, Beijing 100876, China*

(Received 20 March 2024; revised 21 August 2024; accepted 4 September 2024; published 24 September 2024)

Solution-processed molybdenum disulfide (MoS_2) shows promise for tunable photonics and optoelectronics development. However, though scalable, it often leads to devices with inferior performance as a result of its random, discrete nature. In this study, we show via density-functional-theory calculations that the electronic structure of the individual solution-processed nanosheets can be modulated collectively by external electric fields. Particularly, the nanosheets can form Stark ladders, giving variations in the underlying optical processes and thus tunable collective optical properties. We confirm this electro-optical modulation experimentally using solution-processed MoS_2 films with ferroelectric poly(vinylidene fluoride-*co*-trifluoroethylene) [P(VDF-TrFE)] incorporated, and prove that the local polarization fields from P(VDF-TrFE) can modulate the collective optical properties of the MoS_2, specifically, the optical absorption and photoluminescence. Given the scalability of solution processing, our results underpin the potential of electro-optical modulation of solution-processed MoS_2 for tunable photonics and optoelectronics development. To illustrate this potential, we demonstrate solution-processed electroabsorption modulators.

DOI: 10.1103/PhysRevApplied.22.034057

I. INTRODUCTION

Tunable photonics and optoelectronics play a crucial role in sensing, communications, and manufacturing [1]. Mono- and few-layer molybdenum disulfide (MoS_2), with unique electronic structure transition and dynamical optoelectronic process, has attracted significant interest for photonics and optoelectronics innovations. Particularly, the quantum confinement and spontaneous broken translational symmetry enables modulation of the electronic structures and thus the optical processes for tunable photonics and optoelectronics [2–5]. Though promising, large-scale crystalline MoS_2 production remains challenging for the device fabrication [6]. In contrast, solution-processing scales up the production and allows large-area depositions by printing and coating [7–9]. However, the solution-processed MoS_2 is in fact random, discrete networks of mono- and few-layer nanosheets [10, 11]—while the individual nanosheets retain the intrinsic materials physics and properties, the networks exhibit compromised collective properties with distinctly differentiated materials physics.

Understanding the underlying optical processes and properties of solution-processed MoS_2 is pivotal for developing its tunable photonics and optoelectronics. Given the discrete nature, the individual nanosheets can be

*Contact author: gw@bit.edu.cn
†Contact author: ghhu@ee.cuhk.edu.hk

regarded as independent systems, while the networks can be analyzed collectively from the perspective of statistical physics [12]. When subjected to external stimuli, such as light, the collective optical response, $I_{\text{collective}}$, is primarily determined by the structural parameters of the networks and the material physics of the individual nanosheets. Assuming a network comprising N nanosheets, wherein each nanosheet is characterized by M parameters, the collective optical response $I_{\text{collective}}$ can be described as

$$I_{\text{collective}} = \sum_{i}^{N} I_i = \sum_{i}^{N} I_i \left[\left(\prod_{j}^{M} \xi_{ij} \right) \cdot \varphi_i(C; \mathbf{s}_i) \right], \quad (1)$$

where ξ_{ij} is the element of the structural parameter matrix, $\Xi = [\xi_{ij}]_{N\times M}$, representing the jth structural parameter (e.g., the effective area and tilting angle) of the ith nanosheet. The optical response of the ith nanosheet, φ_i, is a function of the incident radiation, $\mathbf{s}_i$, and the modulation approach, C.

Previous studies report that the electronic structures in mono- and few-layer MoS_2 can be modulated by external fields (e.g., magnetic, thermal, and electric fields) [2]. Amongst them, the electric fields are a convenient modulation approach, in particular, for micro-nano device operations. In fact, considering the interplay between the electronic structure and optical transitions, the electric field effect on the optical properties of MoS_2 and the related two-dimensional (2D) materials has been an interesting topic. For example, theoretical [13–15] and experimental [16–20] studies have been made to explore tuning the exciton properties of transition metal dichalcogenides and their heterostructures by electric fields. Note that due to the small Bohr radius and large exciton-binding energy, the fields for dissociation of the strongly bound excitons can be substantial [21]. Besides, previous studies have proposed electric field effect tuning with dielectric engineering [13–15]. However, these studies are based on nanosheet and heterostructure samples prepared by mechanical exfoliation and chemical-vapor deposition. The optical property tuning revealed can thus be deviated from that of solution-processed MoS_2. Nevertheless, as the individual solution-processed nanosheets still maintain a two-dimensional quantum confined configuration, electric fields may still be a viable modulation approach for solution-processed MoS_2. Indeed, in our prior study [22], we show that the electronic structures and thus properties of liquid-phase exfoliated MoS_2 can vary in local electric fields via a quantum confined Stark effect (QCSE).

In this context, we understand that the optical properties of the individual solution-processed MoS_2 nanosheets may be modulated by electric fields; by accumulating the minute variations in the individual nanosheets, substantial changes may render collectively. Note that distinct from our prior study on electronic property modulation [22], here we focus on electro-optical modulation of solution-processed MoS_2. Given the interplay between the electronic structure of matter and its optical properties, the findings in our prior study lay the foundation for us to understand the electro-optical modulation physics and mechanisms. We then explore the application of the electro-optical modulation mechanisms in developing tunable photonics and optoelectronics, for instance, fabricating solution-processed electroabsorption modulators based on MoS_2.

II. OPTICAL PROCESSES IN SOLUTION-PROCESSED MoS_2

Light-matter interactions in semiconductors typically involve reflection, absorption, and transmission (i.e., optical processes without energy conversion), and inelastic scattering of photons and photoluminescence (i.e., optical processes with energy conversion); Fig. 1(a). More explicitly, the transitions in solution-processed MoS_2 include band-to-band direct transition in direct band-gap monolayers [Fig. 1(b)], and phonon-assisted indirect transition in indirect band-gap few layers [Fig. 1(C)].

We study the light-matter interactions in solution-processed MoS_2 using density-functional-theory (DFT) calculations (see Appendix A). Figure S1 within the Supplemental Material [28] shows our calculated band-to-band direct transition in the direct band-gap monolayers that occurs between the conduction-band minimum (CBM) and valence-band maximum (VBM) at $K^{\pm}$. Specifically, the conduction- and valance-band edge states are primarily composed of the d_{z^2} states and $d_{x^2-y^2} \pm id_{xy}$ states of the molybdenum (Mo) atoms, respectively, both mixed with the $p_x \mp ip_y$ states of the sulfur (S) atoms (Fig. S2 within the Supplemental Material [28]). Meanwhile, as shown in Fig. S1 within the Supplemental Material [28], our calculations reveal that the phonon-assisted indirect transition in the indirect band-gap few-layers occurs between the CBM at the halfway point Λ_{min} of the $\Gamma - K$ path and VBM at Γ.

Given that solution-processed MoS_2 is usually four–five layers for the averaged thickness [23,24], we calculate and present in Fig. 1(d) the electronic structure from penta-layer as representative for solution-processed MoS_2. More explicitly, we present in Figs. 1(e)–1(g) the orbital weight of the Mo and S atoms as well as the density of states (DOS). As shown, the CBM at Λ_{min} is primarily composed of Mo: $d_{x^2-y^2} \pm id_{xy}$ states mixed with S: $p_x \mp ip_y$ orbitals, while the VBM at Γ is mainly contributed by Mo d_{z^2} states and S p_z orbitals.

III. FORMATION OF STARK LADDERS IN FEW LAYER MoS_2

When nanostructured materials are applied with an external electric field, F, their electronic structures can

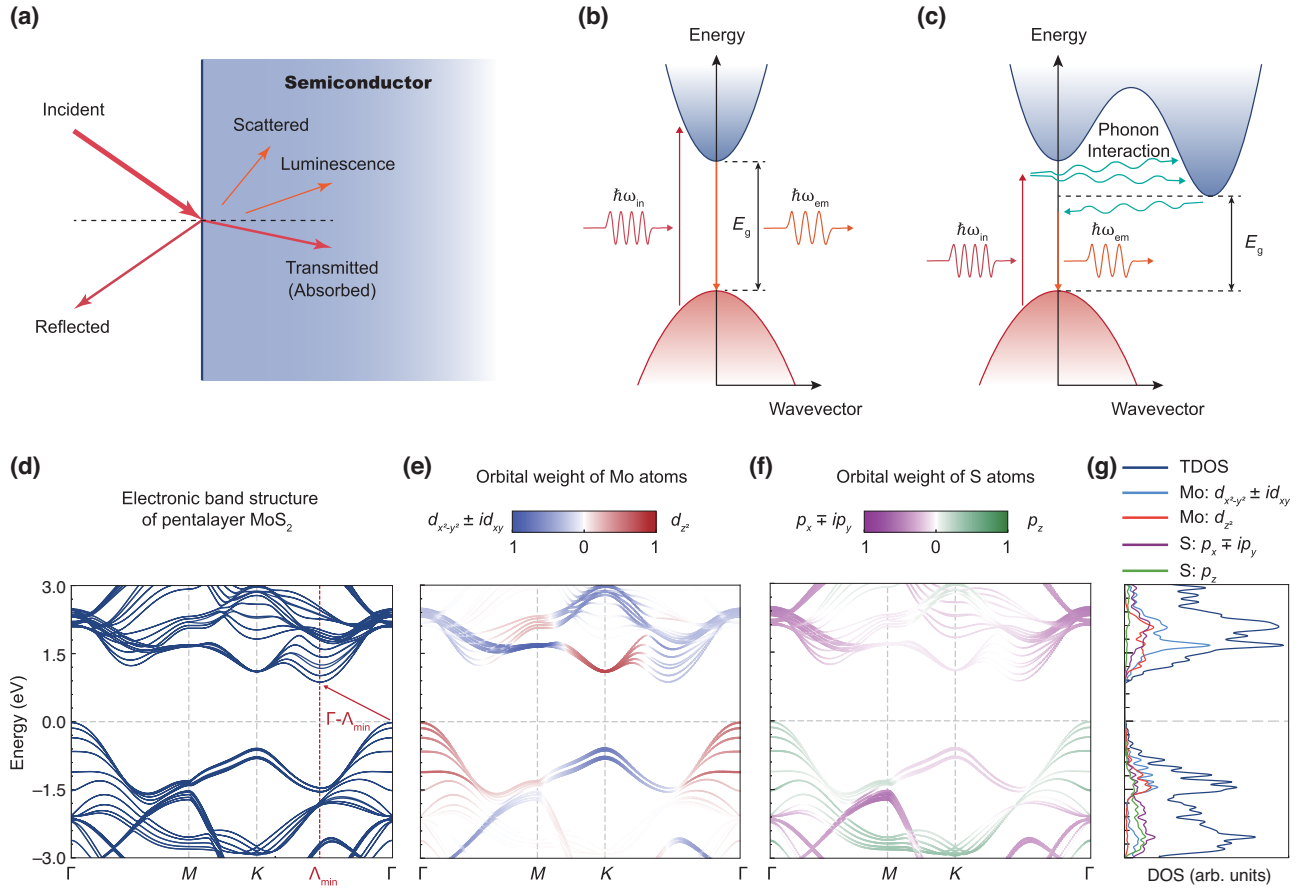

FIG. 1. Optical processes in solution-processed MoS_2. (a) Schematic linear and nonlinear light-semiconductor interactions. (b) Schematic band-to-band transition in direct band-gap semiconductors, and (c) phonon-assisted transition in indirect band-gap semiconductors. (d) Calculated electronic band structure for pentalayer MoS_2, and the orbital weight of the (e) Mo atoms and (f) S atoms, as well as (g) the density of states (DOS). The calculated results from pentalayer MoS_2 are presented as representative for solution-processed MoS_2. See Fig. S1 within the Supplemental Material for the results from the other layer numbers [28].

variate and give electronic band splitting and band-gap reduction, as governed by QCSE [25–27]. The electronic structure evolution due to QCSE exhibits dependence on the dimension of the nanostructured materials. Solution-processed MoS_2 with an an averaged thickness of four–five layers can undergo intense QCSE.

Figure 2(a) schematically illustrates the electronic structure evolution in the few layers—when applied with an external electric field, the few layers with the intralayer spacing can form intralayer dipole moments; once the intralayer dipoles are formed, redistribution of the charges in response to the field can become significant and render intense QCSE. Indeed, intense QCSE is proved in our calculations, with the band-gap significantly narrowed in the few layers; Fig. 2(b). Notably, as shown in Fig. 2(c), the QCSE gets enhanced with the thickness of the few layers. In contrast, as the monolayers lack an intralayer spacing, the formation of effective intralayer dipoles is inhabited, leading to less profound QCSE in the monolayers [Fig. 2(c)].

Therefore, based on the above results and understanding, while the monolayers contribute to the optical properties of solution-processed MoS_2, the few layers primarily govern the optical response changes induced by the QCSE in the electric field, F, as described in Eq. (2):

$$I_{\text{collective}}(F) = I_{\text{monolayer}} + I_{\text{fewlayer}}(F), \tag{2}$$

where $I_{\text{collective}}$, $I_{\text{monolayer}}$ and I_{fewlayer} denote the collective optical response and that from the monolayers and few layers, while the optical response modulation approach is the electric field, F, that is applied to the solution-processed MoS_2. Focusing on the few layers, the electric field, F, can induce a progressive band splitting [Fig. 2(D)], where each of the atomic layers occupies the states at different energy levels (Fig. S3 within the Supplemental Material [28]). The progressive band splitting can eventually lead to the formation of steplike band structures, known as *Stark ladders* [Fig. 3(a)].

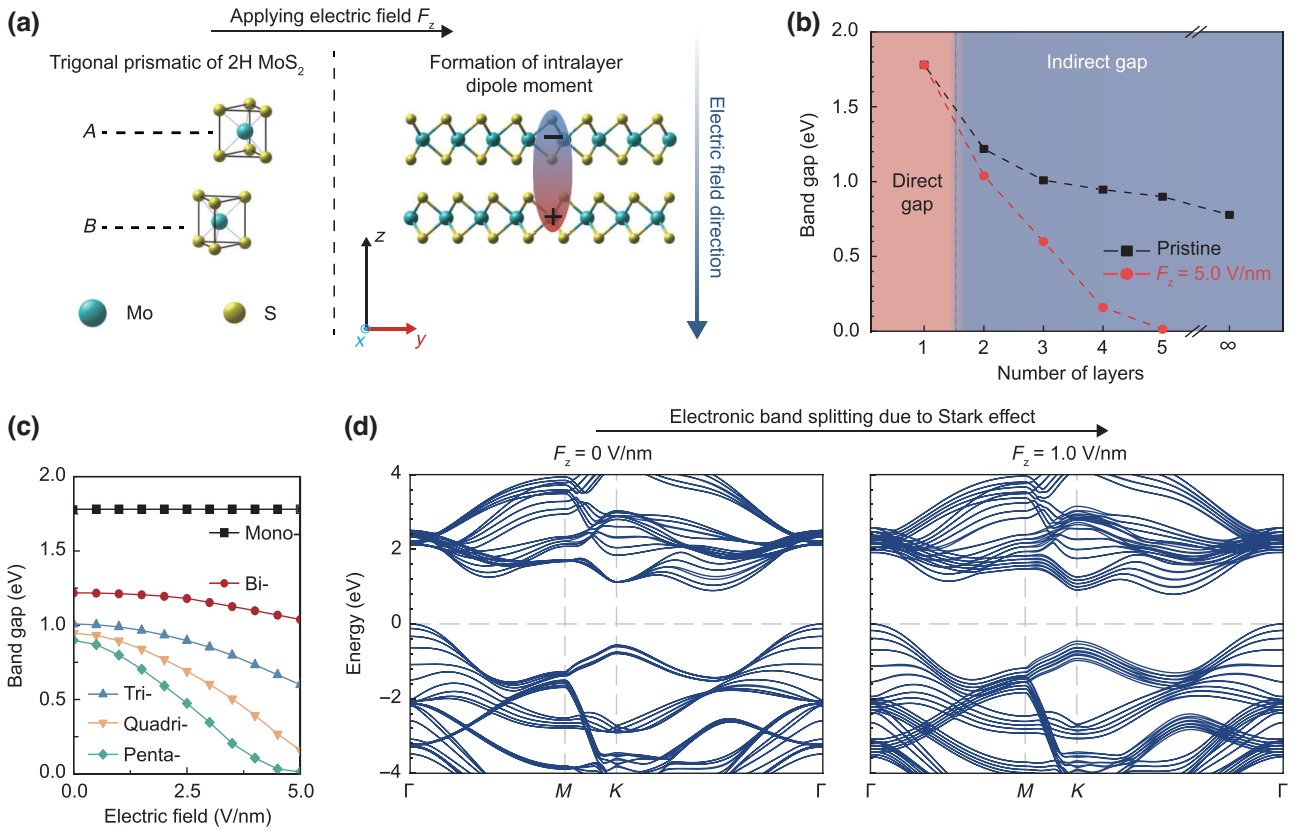

FIG. 2. Electronic structure evolution in solution-processed MoS_2 in external electric fields. (a) Schematic atomic structure of hexagonal (2H) MoS_2, and the formation of intralayer dipole moments in response to an electric field. (b) Calculated band-gap summary for pristine monolayer, few-layer, and bulk MoS_2 without and with an electric field of $F_z = 5.0$ V/nm. (c) Band-gap evolution in monolayer to pentalayer MoS_2 in a longitudinal electric field F_z. (d) Electronic band splitting in pentalayer MoS_2 due to QCSE incurred by the electric field.

Here we note that symmetry operation is excluded in our above DFT calculations. See Appendix B and Note S1 within the Supplemental Material [28] as well as Fig. S4 within the Supplemental Material [28] for our extended DFT calculations with symmetry operation. The symmetry operations in DFT calculations can variate the band-gap narrowing rates and thus, the critical fields to turn off the band-gap [29]. Since the electric field implicitly breaks the symmetry of the mono- and few-layer MoS_2, excluding symmetry in DFT calculations may give more reasonable results, as reported in prior studies [30]. Nevertheless, both energy band splitting and band-gap narrowing are proved in our calculations regardless of the symmetry operation, though large differences in the band splitting and band-gap narrowing rates are observed.

IV. ABSORPTION COEFFICIENT VARIATION AT THE ABSORPTION EDGES

The emergence of Stark ladders can significantly alter the optical processes in solution-processed few-layer MoS_2 nanosheets [31,32]. As such, electric fields and the induced QCSE can potentially modulate the collective optical response of solution-processed MoS_2. Here we note that, without considering the excitonic effects, QCSE can be considered as extreme quantization of the Franz-Keldysh effect in thin-slab structured materials [33]. Therefore, the optical absorption coefficient of solution-processed few layers for photons with energy less than the band-gap, E_g, can be expressed by Eq. (3) [34,35]:

$$\alpha(\omega, F_z) = \frac{1}{2}\alpha(\omega, 0)\exp\left[-\frac{4}{3}\left(\frac{E_g - \hbar\omega}{\hbar\theta_z}\right)^{3/2}\right], \quad (3)$$

where $\alpha(\omega, 0)$ is the initial optical absorption coefficient in the absence of the electric fields, and $\hbar\theta_z = (e^2 F_z{}^2 \hbar^2/2\mu_z)^{1/3}$ is a function of the longitudinal electric fields F_z (see Note S2 within the Supplemental Material [28]). The progressive band splitting and Stark-ladder formation in the few layers can result in a red shift of the collective optical absorption edges, as schematically illustrated in Fig. 3(b). According to Eq. (3), the red shift

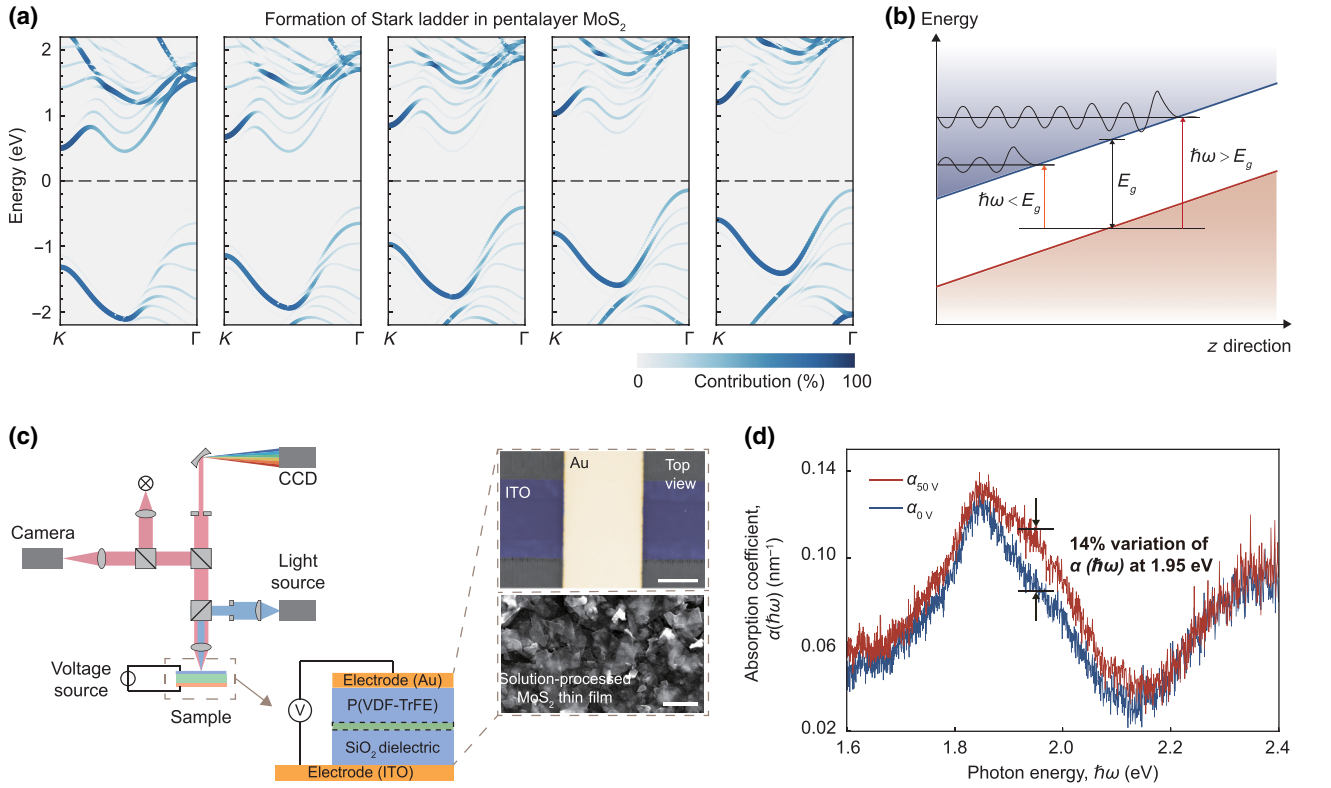

FIG. 3. Electro-optical modulation of solution-processed MoS_2. (a) The formation of Stark ladders in pentalayer MoS_2. (b) Schematic Franz-Keldysh effect due to the Stark ladders in response to the electro-optical modulation. (c) Schematic setup for *in situ* electro-optical characterization of solution-processed MoS_2. The subplots to the right show a detailed sketch illustrating the *in situ* characterization, and a top-view optical microscopic image of a typical solution-processed MoS_2 film for the characterization, as well as a scanning microscopic image showing the deposition of the MoS_2 nanosheets. The green layer as marked corresponds to the deposited solution-processed MoS_2 layer. Scale bars: (top) 500 μm, (bottom) 500 nm. Note a scanning microscopic image of a larger scale is shown in Fig. S9 within the Supplemental Material [28]. (d) Optical absorption coefficient spectrum of the solution-processed MoS_2 film with and without bias.

can lead to changes in the intensity of the optical absorption and reflection for incident light with wavelength $\lambda > hc/E_g$ ($h = 2\pi\hbar$ is the Planck constant, and c is the speed of light), and the most significant changes occur at the initial optical absorption edges.

To experimentally validate our findings, we design a setup [Fig. 3(c)] for *in situ* electro-optical characterizing solution-processed MoS_2 (see Appendix D). Here we prepare MoS_2 via electrochemical exfoliation (see Appendix C). Electrochemical exfoliation can yield large and thin nanosheets [23,24,36], facilitating uniform depositions over large areas, favorable for optical characterizations and device fabrications. Material characterizations confirm that the exfoliated MoS_2 is in the pristine 2H phase (Fig. S5 within the Supplemental Material [28]). Statistical atomic force microscopy (AFM) characterization shows that the averaged thickness of the exfoliated MoS_2 is 3.57 nm (about four–five layers, in alignment with our DFT calculations), and the averaged lateral dimension is 606.6 nm; Fig. S6 within the Supplemental Material [28]. The exfoliated MoS_2 is used to prepare films in a structure of $ITO/SiO_2/MoS_2/P(VDF\text{-}TrFE)/Au$ for convenient *in situ* electro-optical characterization, as shown by the subplots in Fig. 3(c). The ferroelectric P(VDF-TrFE) is incorporated to introduce the local polarization fields for inducing QCSE [37], while the SiO_2 is evaporated to prevent current leakages. Note that layer-by-layer spin coating and annealing are used for depositing the MoS_2 and P(VDF-TrFE), so as to avoid interlayer wetting and diffusion during deposition [22].

Using the *in situ* electro-optical characterization setup, we investigate field-induced modulation of the collective optical properties of solution-processed MoS_2. Indeed, as revealed in Fig. 3(d), the collective optical absorption coefficient from a typical solution-processed MoS_2 film varies in response to the bias applied. Notably, for the photons with energy less than 2.1 eV, the film exhibits an increased absorption. The maximum change (i.e., approximately 14 % variation) in the absorption coefficient occurs at approximately 1.95 eV, which is between the A (approximately 1.84 eV) and B (approximately 2.00 eV) excitonic absorption peaks of MoS_2. Therefore, the experimental

results validate our theoretical findings that the collective optical properties of solution-processed MoS_2 can vary at the absorption edges due to QCSE.

V. ELECTRIC-FIELD-INDUCED PHOTOLUMINESCENCE QUENCHING

The optical processes discussed so far do not involve energy conversion, such as photon-electron, photon-phonon, and photon-phonon-electron interactions. However, the QCSE-induced electronic structure evolution in solution-processed MoS_2 can also impact the energy-conversion processes. Here we investigate the photoluminescence emission as a demonstration. Unlike optical absorption, photon emission in MoS_2 typically occurs through the relaxation of the excited electrons and holes, followed by their recombination and subsequent photon emission [38,39]. The excited electron-hole pairs, however, tend to separate driven by the electric fields applied, as schematically illustrated in Figs. 4(a) and 4(b). As a result, the photon emission, measured as the photoluminescence intensity from the solution-processed MoS_2 films, can be decreased by the applied bias.

The decrease of the photoluminescence intensity, i.e., photoluminescence quenching, has been well studied in nanostructures [40,41], including 2D materials and their heterostructures [42]. Notably, these studies use straightforward models based on wave-function overlap to describe the electronic band-structure evolution in external fields. Compared to these systems, solution-processed 2D materials are essentially disordered, discrete percolative networks, and yet maintain a crystalline structure on the microscopic scale. Given this, a straightforward model based on wave-function overlap may not reveal the profound interactions between the solution-processed 2D material nanosheets. To understand photoluminescence quenching in solution-processed MoS_2, the individual nanosheets can be regarded as independent systems and described by straightforward models, while the networks can be analyzed collectively from the perspective of statistical physics. In this consideration, we will first need to understand the QCSE-induced electro-optical processes in the solution-processed MoS_2 nanosheets.

As discussed, the QCSE induced electro-optical processes in solution-processed MoS_2 are primarily governed by the indirect-band-gap few layers. Here we note that,

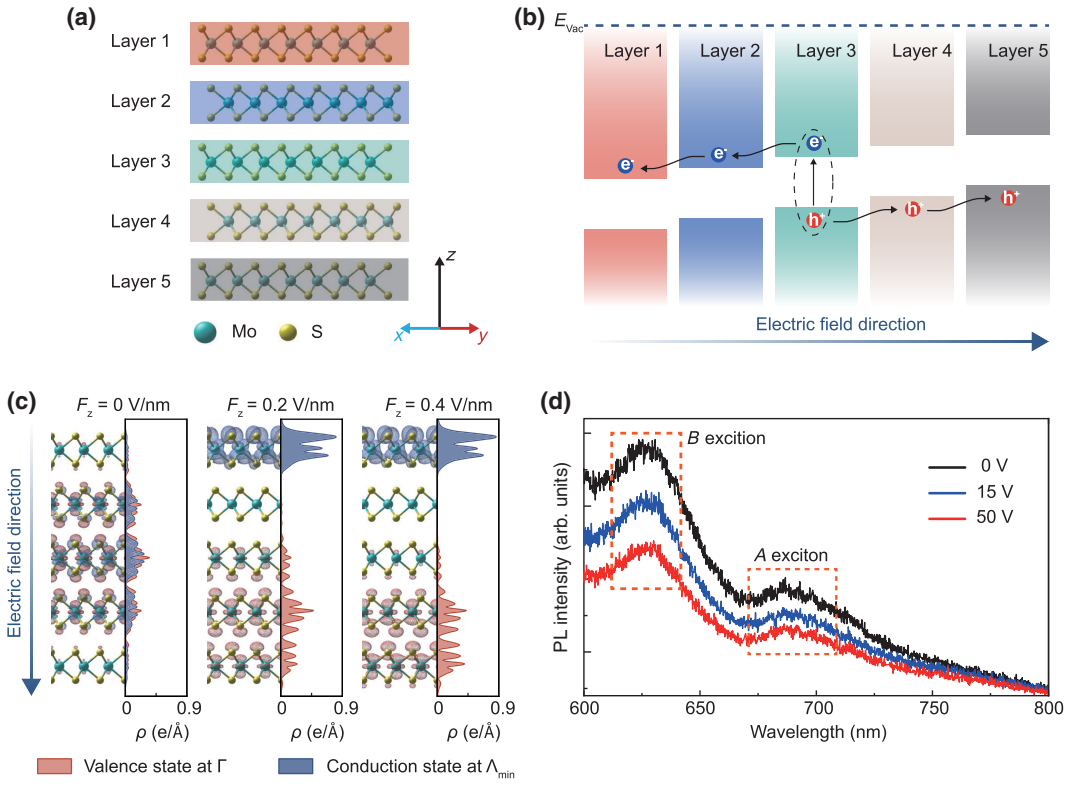

FIG. 4. Field-induced photoluminescence quenching in solution-processed MoS_2. (a) Structure of pentalayer MoS_2. (b) Schematic electron-hole pair separation in a MoS_2 nanosheet due to the Stark ladder in an external electric field, showing the separation and propagation of an electron-hole pair. (c) The calculated spatial distribution of the valence and conduction states in pentalayer MoS_2. Substantial spatial separation takes place in response to the external electric field, showing the redistribution of electrons and holes. (d) *In situ* experimental photoluminescence spectrum of the solution-processed MoS_2 film, showing electro-optical photoluminescence quenching.

coexisting with the phonon-assisted indirect transitions, direct transitions are not forbidden in the few layers [43,44]. Particularly, since the indirect transitions involve phonons, the probability is limited [35]. On the other hand, though the direct K − K transition is weakened due to the direct to indirect transformation from mono- to few layer, the probability can still be significant and dominate the photoluminescence process [43]. Given this, we focus on the direct transition. See Note S3 within the Supplemental Material [28] for discussion on the indirect transition involving the interaction of phonons.

In direct transition, the excitonic recombination probability per unit time in individual MoS_2 nanosheets can be expressed as [35]

$$\gamma_{c\to v} = \frac{2\pi}{\hbar}\cdot\left(\frac{eA_0}{m}\right)^2 \sum_{\mathbf{k}_c,\mathbf{k}_v} |P_{cv,\parallel}\cdot S_{cv,\perp}|^2 \times \sum_{\varrho} |\phi_\varrho(0)|^2 \delta[(E_g + E_\varrho) - \hbar\omega], \quad (4)$$

where A_0 is the emission intensity, $\phi_\varrho(0)$ is the wave function of the exciton with zero relative motion, E_ϱ is the energy of the exciton, and $P_{cv,\parallel}$ is the transition dipole moment of the carrier recombination process. As the translational symmetry in the z direction is broken, the periodical interaction is limited to the two-dimensional atomic plane (xOy plane). And, the optical transition in the z direction is decided by the overlap integral between conduction and valence states, $S_{cv,\perp}$, as described by Eq. (5):

$$S_{cv,\perp} = \int_{L_z} \phi_c^* \phi_v dz = \int_{L_z} \phi_c \phi_v dz, \quad (5)$$

where ϕ_c and ϕ_v are the wave functions of conduction and valence states, respectively, and L_z is the thickness of the nanosheets. Similarly, this is also true for the phonon-assisted indirect transition (Note S3 within the Supplemental Material [28]). Therefore, as revealed by our calculations [Fig. 4(c)], in the presence of an external electric field, the wave functions of conduction and valence states spatially separate, leading to the reduction in the overlap integral $S_{cv,\perp}$. As such, the corresponding excitonic recombination probability per unit time in the few-layer MoS_2 nanosheets decreases. As discussed, the minute decrease can accumulate and quench the collective photoluminescence. See Note S4 within the Supplemental Material [28] for more detailed discussion.

To validate photoluminescence quenching in solution-processed MoS_2, we perform *in situ* photoluminescence characterization. As shown in Fig. 4(d), the photoluminescence intensity decreases as the bias increases. Specifically, as observed, the two characteristic photoluminescence peaks corresponding to the emission of the *A* (approximately 1.80 eV) and *B* (approximately 1.98 eV) excitons in MoS_2 exhibit significant decreases. Note that the measured full width at half maximum of the photoluminescence peaks (approximately 70 nm) is considerably broader than those reported for the mono- and few-layer crystalline MoS_2 nanosheets [45]. This broadening is attributed to the mixture of nanosheets with various thicknesses in the solution-processed MoS_2. Besides, previous studies report that the photoluminescence from few-layer MoS_2 may red shift due to the Stark effect [25,30]. However, no obvious red shifting is observed during quenching in our characterization. As discussed, the monolayers primarily dominate the photoluminescence of the solution-processed MoS_2, and as the monolayers do not undergo significant Stark effect and band-gap reduction [Figs. 2(b) and 2(c)], the overall photoluminescence does not render notable red shifting. However, as observed, the photoluminescence peaks are broadened during quenching, suggesting the photoluminescence from the few layers may have red shifted. To study this further, we perform multipeak fitting [46] of the photoluminescence spectra (Fig. S7 within the Supplemental Material [28]), and the two emerging red-shifted wave packets suggest a red-shifting photoluminescence from the few layers. Therefore, we understand that the photoluminescence from the few layers do red shift during quenching, but the red shifting is overshadowed by the relatively intense photoluminescence from the monolayers. Nevertheless, the *in situ* electrophotoluminescence characterization confirms the photoluminescence quenching and proves that electric fields can be employed to effectively modulate the collective energy-conversion optical processes in solution-processed MoS_2.

VI. SOLUTION-PROCESSED ELECTROABSORPTION MODULATORS

An effective electro-optical modulation of solution-processed MoS_2 holds the potential for tunable optical device development. To illustrate this potential, as an example, we fabricate electroabsorption modulators (EAMs). Capable of actively modulating the optical fields with bias, EAMs are an indispensable technology for datacom and optical computing [47,48]. However, current EAMs demand high-precision manufacturing of highly crystalline optical materials, such as silicon, lithium niobate, and III-V semiconductors. This leads to the high cost of the EAMs, a stringent barrier for the widespread applications of EAMs [49,50]. Continuous efforts have been made to explore alternative optical materials and fabrication methods for scaled-up, more accessible EAMs.

Optimizing our solution-processed MoS_2 film development, we fabricate the EAMs, as shown in Fig. 5(a) (see also Fig. S8 within the Supplemental Material [28]). As observed in Figs. 5(b)–5(d), after optimization, the EAMs develop distinct layer-by-layer interfaces. Upon

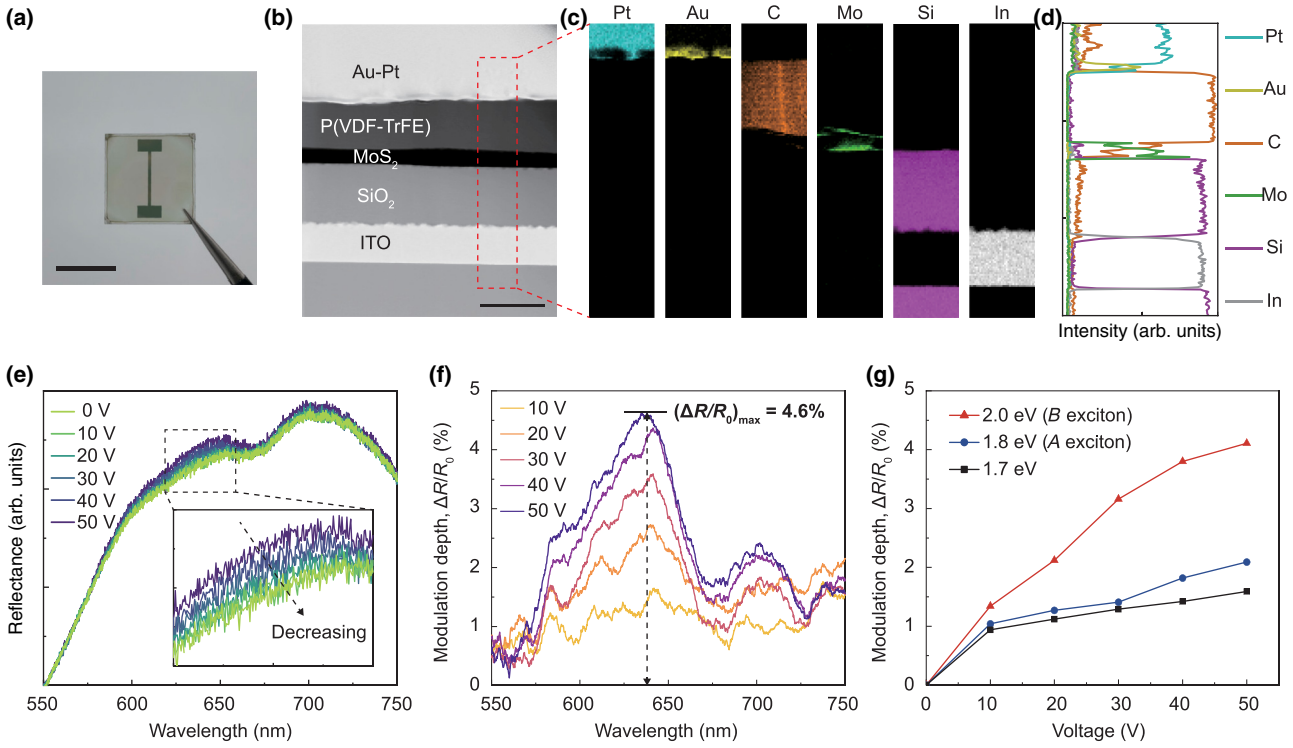

FIG. 5. Solution-processed MoS_2 electroabsorption modulators (EAMs). (a) Photo of a typical device. (b) Cross-section scanning transmission electron microscopic image of the device, and the corresponding (c) energy-dispersive x-ray area mapping and (d) linear profile. The device is in an ITO/SiO_2/MoS_2/P(VDF-TrFE)/Au structure. (e) *In situ* electroreflectance spectrum of the device under the different biases, and (f) the corresponding static absorption modulation depth $\Delta R/R_0$ calculated from the *in situ* electroreflectance. (g) Summary of the modulation depth of the device to the characteristic photon energies, i.e., the *A*, *B* excitons and an energy slightly smaller than the absorption edge of the solution-processed MoS_2. Scale bars: (a) 10 mm, (b) 500 nm.

in situ electro-optical characterization, we select reflective mode as the back electrode of gold is opaque to visible light. This gives the EAMs a zero transmissivity ($T = 0$), while the transparent front electrode of ITO and insulating layer of SiO_2 allow measurement of the reflection from the MoS_2 sandwiched in the EAMs. Neglecting the minimal optical absorption by ITO and SiO_2, the optical reflectivity (R) and absorptivity (A) of the MoS_2 give $R + A = 1$. Consequently, the change in the absorption by the MoS_2 can be interpreted as the change in the reflection using Eq. (6):

$$\begin{aligned}\Delta I_{\text{reflected}}(V,\lambda) &= I_{\text{reflected}}(V,\lambda) - I_{\text{reflected}}(0,\lambda)\\ &= -\Delta I_{\text{absorbed}}(V,\lambda),\end{aligned} \tag{6}$$

where $I_{\text{reflected}}$ denotes the measured intensity of the reflection with wavelength λ, and ΔI represents the intensity changes in optical absorption and reflection.

As shown in Fig. 5(e), the reflectance of a typical MoS_2 EAM decreases in response to the applied bias. This is consistent with the predicted rise in the absorption coefficient according to our calculations above. More explicitly, as shown in Fig. 5(f), the spectrum of the static modulation depth ($\Delta R/R_0$) as calculated from Fig. 5(e) indicates that the EAM exhibits a reflection modulation for the incident light with wavelength >575 nm (corresponding to a photon energy around and below the characteristic *A* and *B* excitons). Further, as observed, the modulation strength is most pronounced at the absorption edges (near the *A* and *B* exciton locations), and it increases with the applied bias, as shown in Fig. 5(g). Note that the maximal modulation depth of the EAM is about 4.6 % at approximately 638 nm, corresponding to the maximum change in the absorption coefficient at 1.95 eV [Fig. 5(f)]. As such, the maximal extinction ratio of the EAM can be estimated as $(R_{\text{on/off}})_{\max} = 4.343 \times [\alpha_{50\text{V}}(1.95\text{ eV}) - \alpha_{0\text{V}}(1.95\text{ eV})] \times L$, where L is the thickness of the MoS_2 film (approximately 100 nm). The estimation yields an extinction ratio of approximately 8.25 dB. The relative static modulation efficiency, $(R_{\text{on/off}})_{\max}/\Delta V$, is thus estimated as approximately 0.165 dB/V.

While proving the functionality of EAMs, our solution-processed MoS_2 EAMs with the exhibited optical modulation performance are not yet comparable to state-of-the-art reports [51,52]. Much work is needed to improve the modulation depth, the extinction ratio, and the modulation efficiency via advancements in materials processing and device fabrication as well as metasurface designs [53].

Nevertheless, our EAMs prove the feasibility of electro-optical modulation of solution-processed MoS_2 for scaled-up tunable photonics and optoelectronics.

VII. CONCLUSION

We have demonstrated electro-optical modulation of solution-processed MoS_2. Through extensive DFT calculations, we have revealed that the optical properties of solution-processed MoS_2 can undergo collective changes when subjected to electric fields. The changes are attributed to the collective evolution of the underlying electronic structure in the randomly networked nanosheets. This electro-optical modulation is experimentally confirmed, where we prove solution-processed MoS_2 exhibits notable electric-field-induced modulation of the optical absorption and photoluminescence. Employing this electro-optical modulation approach, we have demonstrated EAMs, as an example to illustrate the potential for developing tunable photonics and optoelectronics from solution-processed MoS_2. The prototyped EAMs exhibit a static modulation depth of 4.6 %, an extinction ratio of 8.25 dB, and a static modulation efficiency of 0.165 dB/V. Though further improvements in materials processing and device fabrication as well as metasurface designs are required to enhance the optical modulation performance, this demonstration has proved the feasibility of developing solution-processed tunable photonics and optoelectronics of MoS_2.

Here we would like to note that the DFT calculations in our study assume the MoS_2 nanosheets are placed in vacuum (see Appendix B). However, the dielectric environment can seriously impact the electro-optical modulation of the MoS_2 nanosheets [54–56], for example, dielectric screening and weakening of the effect of external electric fields [57]. Besides the electric-field-induced QCSE, the electro-optical modulation may partially originate from the moving charges from the surrounding insulators as driven by the electric fields [58]. Regarding the PL quenching observed, besides the electro-optical modulation, doping-induced trions in the solution-processed MoS_2 nanosheets may be a possible mechanism. Doping induced trions can broaden and redshift the neutral exciton emission [59,60]. However, deeper insights into the dielectric environment, the moving charges from the surrounding insulators, and the doping-induced trions require further detailed investigations. Nevertheless, a deeper insight will be key to the further optimization of the electro-optical modulation and to promote the performance of the solution-processed electro-optic modulators towards practical applications.

ACKNOWLEDGMENTS

G.W. acknowledges support from NSFC (Grant No. 12074033), G.H.H. from CUHK (Grant No. 4055115), RGC (Grant No. 24200521), and NSFC (Grant No. 62304196), Yang Liu from SHIAE (Grant No. RNE-p3-21), J.F.P. and Y.Y.W. from RGC (Grant No. 24200521), Yue Lin from NSFC (Grant No. 52273029), Fujian Science & Technology Innovation Laboratory for Optoelectronic Information of China (Grant No. 2021ZZ119), Pilot Project of Fujian Province (Grant No. 2022H0037) and Natural Science Foundation of Fujian Province for Distinguished Young Scholars (Grant No. 2023J06045), T.M. from PolyU (Grant No. P0042991), P.P.Z. from BUPT (Startup Funding), and X.L.C. from NSFC (Grant No. 62275117) and Shenzhen Basic Research Program (Grant No. 20220815162316001). The authors thank Shenzhen Cloud Computing Center, National Supercomputing Center and the High-Performance Computing Platform of BUPT for providing the high-performance computing clusters services, and Miss Xiaolin Liu for discussions on the *ab initio* calculations.

APPENDIX A: DENSITY-FUNCTIONAL-THEORY CALCULATIONS

Vienna *ab initio* simulation package (VASP) [61] is adopted to perform the density-functional-theory calculations. Projector augmented-wave pseudopotential [62] is used to describe the interaction between the ionic core and valence electrons. The generalized gradient approximation functional in the Perdew-Burke-Ernzerhof scheme [63] is used to describe the exchange-correlation (XC) energy between the electrons. The Mo ($4p$, $5s$, dd) states and S (s, p) states are treated as valence states. The plane-wave cutoff energy is set to be 500 eV. van der Waals correction is carried out during the crystal structural relaxation using the DFT-D3(BJ) method [64,65]. The structure of all the systems is fully optimized until the residual force on the atoms is less than 0.01 eV/Å. For the broken translational symmetry in the solution-processed MoS_2 nanosheets, we use a slab geometry with a 22-Å vacuum layer to prevent the interaction between the nanosheets. For the self-consistent iteration, the convergence tolerance between the successive steps is set as 1×10^{-6} eV. The Monkhorst-Pack method is used to generate the k-point grid. All the solution-processed MoS_2 nanosheets use a $14 \times 14 \times 1$, $21 \times 21 \times 1$, and $31 \times 31 \times 1$ grid for the structural relaxation, self-consistent calculation, and calculation of density of states, respectively. The visualization of the atomic structure, molecular orbitals, and charge density are carried out via VESTA [66].

APPENDIX B: SIMULATION OF THE STARK EFFECT

In the simulation of the Stark effect in solution-processed MoS_2, the electric field is applied by introducing dipole sheet within the vacuum layer. Considering that the electric field applied to the solution-processed MoS_2

is mediated by the dipole polarization of the insulating SiO_2 and ferroelectric P(VDF-TrFE) layer, setting a dipole sheet as electric field source is reasonable. Note that, although the composition of the solution-processed MoS_2 is random, the orientation of the nanosheets within is ordered to some extent in a microscopic scale. As demonstrated in Fig. S6 within the Supplemental Material [28], the averaged lateral dimension of the MoS_2 nanosheets is about 170 times of their averaged thickness. Vertical alignment of the nanosheets is highly unstable. Indeed, the nanosheets are largely placed horizontally while randomly connect with the neighboring nanosheets, as demonstrated in Fig. 3(c) (see also Fig. S9 within the Supplemental Material [28]), where the top-view scanning electron microscopic image show ordered orientation of the nanosheets in a microscopic scale. Therefore, a vertically applied electric field is suitable for the calculations and can give an effective explanation to the results observed.

During calculation of the charge density under the external electric fields, note that the symmetry operation can play a significant role. To figure out its relevance, in Fig. S4 within the Supplemental Material [28], we examine the impact of symmetry operation on the electric field effect on bilayer MoS_2 nanosheets, with or without considering the spin-orbit coupling (SOC). The effect of SOC on the Stark effect of bilayer MoS_2 is negligible, while symmetry can lead to major differences. This may originate from the symmetry confinement that traps the electronic structure of the system inside a local minimum, leading to an inappropriate charge density configuration.

In a general DFT calculation protocol, including symmetry operation is set as default in VASP (ISYM = 2) [67]. Under this setup, VASP firstly determines the symmetry characteristic (space group) based on the configuration of the target system, and uses the symmetry operators of the corresponding space group to directly symmetrize the target charge density. As such, VASP can reduce the computation load. In the case of mono- and few-layer MoS_2, odd number of layers MoS_2 has space group $P\bar{6}m2$ belonging to point group D_{3h}, while even number of layers MoS_2 has space group $P\bar{3}m1$ belonging to point D_{3d} [68,69]. Point group D_{3h} has a horizontal mirror operator σ_h, and point group D_{3d} has an inversion center i [68,69]. In normal cases, when the symmetry operation is on, these two operators reflect the charge density along the z direction across the horizontal plane located at the middle of the unit cell specularly and inversely, respectively. Instead of directly calculating the charge density of the whole structure, this simplification by symmetry operation is more effective.

However, the introduction of the vertical electric field can surely break the mirror and inversion symmetries. Although the calculation results of including symmetry operation (Fig. S4 within the Supplemental Material [28]) is consistent with previous theoretical studies [26,70], the results of excluding symmetry operation (Fig. 2; Fig. S4A, D–I within the Supplemental Material [28]) is closer to the experimental reports [30]. As such, deactivating symmetry operation (ISYM $= -1/0$) is adopted in our study and presented in the main context. The choice of symmetrizing the k-point mesh instead of directly symmetrizing the charge density may also work, but this is not investigated in our research. It is observed that although the band-gap reduction rate, i.e., the linear Stark effect coefficient, is deviated from that reported in previous studies [26,70], the evolution of the electronic structure redistribution and the resultant band splitting alongside band-gap reduction in response to the electric fields in the few-layer MoS_2 is confirmed and consistent.

APPENDIX C: SOLUTION-PROCESSING AND DEVICE FABRICATION

Solution-processed MoS_2 suspension is prepared by electrochemical exfoliation of bulk MoS_2 crystals (SPI Supplies) for spin-coating deposition. The electrochemical exfoliation process follows the method reported in Ref. [24]. P(VDF-TrFE) (70:30) (Sigma) is dissolved in methyl ethyl ketone (MEK) (Sigma) via magnetic stirring to form a 60 mg/ml solution for spin coating (Fig. S10 within the Supplemental Material [28]). SiO_2 is deposited onto the ITO substrate via e-beam evaporation. The solution-processed MoS_2 suspension and P(VDF-TrFE) dispersion are then deposited onto the ITO/SiO_2 substrate through a layer-by-layer spin-coating process, followed by a heat treatment to remove the residual solvents. Opaque back-contact Au electrode is deposited through e-beam evaporation on the top to complete the device fabrication.

APPENDIX D: *IN SITU* ELECTRO-OPTICAL CHARACTERIZATIONS

The *in situ* electro-optical characterizations are performed at room temperature using a 532-nm continuous laser excitation with a diffraction-limited excitation beam diameter of 1 μm. The excitation light is filtered by a 532-nm-long pass filter (Semrock). The photoluminescence signal light is separated by a 300 g/mm grating, and then received by a liquid nitrogen-cooled charge-coupled device. The *in situ* electro-optical characterizations under bias are implemented by Keithley 2636B.

[1] G. T. Reed, G. Mashanovich, F. Y. Gardes, and D. J. Thomson, Silicon optical modulators, Nat. Photonics **4**, 518 (2010).

[2] K. S. Novoselov, A. Mishchenko, A. Carvalho, and A. H. Castro Neto, 2D materials and van der Waals heterostructures, Science **353**, 6298 (2016).

[3] C. H. Ahn, A. Bhattacharya, M. Di Ventra, J. N. Eckstein, C. D. Frisbie, M. E. Gershenson, A. M. Goldman, I. H. Inoue, J. Mannhart, A. J. Millis, *et al.*, Electrostatic modification of novel materials, Rev. Mod. Phys. **78**, 1185 (2006).

[4] F. Xia, H. Wang, D. Xiao, M. Dubey, and A. Ramasubramaniam, Two-dimensional material nanophotonics, Nat. Photonics **8**, 899 (2014).

[5] K. F. Mak and J. Shan, Photonics and optoelectronics of 2D semiconductor transition metal dichalcogenides, Nat. Photonics **10**, 216 (2016).

[6] S. Wang, X. Liu, M. Xu, L. Liu, D. Yang, and P. Zhou, Two-dimensional devices and integration towards the silicon lines, Nat. Mater. **21**, 1225 (2022).

[7] T. Y. Zou and Y. Y. Noh, Solution-processed 2D transition metal dichalcogenides: Materials to CMOS electronics, Acc. Mater. Res. **4**, 548 (2023).

[8] S. Pinilla, J. Coelho, K. Li, J. Liu, and V. Nicolosi, Two-dimensional material inks, Nat. Rev. Mater. **7**, 717 (2022).

[9] S. Conti, G. Calabrese, K. Parvez, L. Pimpolari, F. Pieri, G. Iannaccone, C. Casiraghi, and G. Fiori, Printed transistors made of 2D material-based inks, Nat. Rev. Mater. **8**, 651 (2023).

[10] A. C. Kelly, D. O'Suilleabhain, C. Gabbett, and J. N. Coleman, The electrical conductivity of solution-processed nanosheet networks, Nat. Rev. Mater. **7**, 217 (2022).

[11] M. Nasilowski, B. Mahler, E. Lhuillier, S. Ithurria, and B. Dubertret, Two-dimensional colloidal nanocrystals, Chem. Rev. **116**, 10934 (2016).

[12] M. Gerosa and C. E. Bottani, Multiple light scattering and near-field effects in a fractal treelike ensemble of dielectric nanoparticles, Phys. Rev. B **87**, 195312 (2013).

[13] T. G. Pedersen, Exciton Stark shift and electroabsorption in monolayer transition-metal dichalcogenides, Phys. Rev. B **94**, 125424 (2016).

[14] S. Haastrup, S. Latini, K. Bolotin, and K. S. Thygesen, Stark shift and electric-field-induced dissociation of excitons in monolayer MoS_2 and hBN/MoS_2 heterostructures, Phys. Rev. B **94**, 041401(R) (2016).

[15] T. G. Pedersen, S. Latini, K. S. Thygesen, H. Mera, and B. K. Nikolić, Exciton ionization in multilayer transition-metal dichalcogenides, New J. Phys. **18**, 073043 (2016).

[16] N. Peimyoo, T. Deilmann, F. Withers, J. Escolar, D. Nutting, T. Taniguchi, K. Watanabe, A. Taghizadeh, M. F. Craciun, K. S. Thygesen, *et al.*, Electrical tuning of optically active interlayer excitons in bilayer MoS_2, Nat. Nanotechnol. **16**, 888 (2021).

[17] A. Steinhoff, M. Rösner, F. Jahnke, T. O. Wehling, and C. Gies, Influence of excited carriers on the optical and electronic properties of MoS_2, Nano Lett. **14**, 3743 (2014).

[18] A. J. Giles, S. Dai, O. J. Glembocki, A. V. Kretinin, Z. Sun, C. T. Ellis, J. G. Tischler, T. Taniguchi, K. Watanabe, M. M. Fogler, *et al.*, Imaging of anomalous internal reflections of hyperbolic phonon-polaritons in hexagonal boron nitride, Nano Lett. **16**, 3858 (2016).

[19] M. Massicotte, F. Vialla, P. Schmidt, M. B. Lundeberg, S. Latini, S. Haastrup, M. Danovich, D. Davydovskaya, K. Watanabe, T. Taniguchi, *et al.*, Dissociation of two-dimensional excitons in monolayer WSe_2, Nat. Commun. **9**, 1633 (2018).

[20] B. Zhu, K. Xiao, S. Yang, K Watanabe, T Taniguchi, and X Cui, In-plane electric-field-induced orbital hybridization of excitonic states in monolayer WSe_2, Phys. Rev. Lett. **131**, 036901 (2023).

[21] G. Wang, A. Chernikov, M. M. Glazov, T. F. Heinz, X. Marie, T. Amand, and B. Urbaszek, Excitons in atomically thin transition metal dichalcogenides, Rev. Mod. Phys. **90**, 021001 (2018).

[22] S. Liu, X. Fan, Y. Wen, P. Liu, Y. Liu, J. Pei, W. Yang, L. Song, D. Pan, P. Zhang, *et al.*, Conduction modulation of solution-processed 2D materials, Adv. Electron. Mater. **10**, 2300799 (2024).

[23] G. H. Hu, L. S. Yang, Z. Y. Yang, Y. Wang, X. Jin, J. Dai, Q. Wu, S. Liu, X. Zhu, X. Wang, *et al.*, A general ink formulation of 2D crystals for wafer-scale inkjet printing, Sci. Adv. **6**, 33 (2020).

[24] Z. Y. Lin, Y. Liu, U. Halim, M. Ding, Y. Liu, Y. Wang, C. Jia, P. Chen, X. Duan, C. Wang, *et al.*, Solution-processable 2D semiconductors for high-performance large-area electronics, Nature **562**, 254 (2018).

[25] N. Leisgang, S. Shree, I. Paradisanos, L. Sponfeldner, C. Robert, D. Lagarde, A. Balocchi, K. Watanabe, T. Taniguchi, X. Marie, *et al.*, Giant stark splitting of an exciton in bilayer MoS_2, Nat. Nanotechnol. **15**, 901 (2020).

[26] A. Ramasubramaniam, D. Naveh, and E. Towe, Tunable band gaps in bilayer transition-metal dichalcogenides, Phys. Rev. B **84**, 205325 (2011).

[27] Y. P. Liu, Z. Z. Qiu, A. Carvalho, Y. Bao, H. Xu, S. J. R. Tan, W. Liu, A. H. Castro Neto, K. P. Loh, and J. Lu, Gate-tunable giant Stark effect in few-layer black phosphorus, Nano Lett. **17**, 1970 (2017).

[28] See Supplemental Material at http://link.aps.org/supplemental/10.1103/PhysRevApplied.22.034057 for a more detailed discussion on the symmetry settings in VASP and the deraivation process of formulas posted in the main text, alongside supporting data and schematics explaining the ideas of this article.

[29] Y. Chen, J. Liu, J. Yu, Y. Guo, and Q. Sun, Symmetry-breaking induced large piezoelectricity in Janus tellurene materials, Phys. Chem. Chem. Phys. **21**, 1207 (2019).

[30] J. Klein, J. Wierzbowski, A. Regler, J. Becker, F. Heimbach, K. Müller, M. Kaniber, and J. J. Finley, Stark effect spectroscopy of mono- and few-layer MoS_2, Nano Lett. **16**, 1554 (2016).

[31] D. Berghoff, J. Bühler, M. Bonn, A. Leitenstorfer, T. Meier, and H. Kim, Low-field onset of Wannier-Stark localization in a polycrystalline hybrid organic inorganic perovskite, Nat. Commun. **12**, 5719 (2021).

[32] E. E. Mendez, F. Agullorueda, and J. M. Hong, Stark localization in GaAs-GaAlAs superlattices under an electric field, Phys. Rev. Lett. **60**, 2426 (1988).

[33] D. A. B. Miller, D. S. Chemla, and S. Schmittrink, Relation between electroabsorption in bulk semiconductors and in quantum wells: The quantum-confined Franz-Keldysh effect, Phys. Rev. B **33**, 6976 (1986).

[34] J. Hader, N. Linder, and G. H. Dohler, **k**·**p** theory of the Franz-Keldysh effect, Phys. Rev. B **55**, 6960 (1997).

[35] C. Hamaguchi, *Basic Semiconductor Physics* (Springer, Berlin, Heidelberg, 2017), 3rd ed.

[36] J. N. Coleman, M. Lotya, A. O'Neill, S. D. Bergin, P. J. King, U. Khan, K. Young, A. Gaucher, S. De, R. J. Smith, *et al.*, Two-dimensional nanosheets produced by liquid exfoliation of layered materials, Science **331**, 568 (2011).

[37] G. J. Wu, B. B. Tian, L. Liu, W. Lv, S. Wu, X. Wang, Y. Chen, J. Li, Z. Wang, S. Wu, *et al.*, Programmable transition metal dichalcogenide homojunctions controlled by nonvolatile ferroelectric domains, Nat. Electron. **3**, 43 (2020).

[38] H. Y. Shi, R. S. Yan, S. Bertolazzi, J. Brivio, B. Gao, A. Kis, D. Jena, H. G. Xing, and L. Huang, Exciton dynamics in suspended monolayer and few-layer MoS_2 2D crystals, ACS Nano **7**, 1072 (2013).

[39] R. Wang, B. A. Ruzicka, N. Kumar, M. Z. Bellus, H.-Y. Chiu, and H. Zhao, Ultrafast and spatially resolved studies of charge carriers in atomically thin molybdenum disulfide, Phys. Rev. B **86**, 045406 (2012).

[40] Y. Horikoshi, A. Fischer, and K. Ploog, Photoluminescence quenching in reverse-biased $Al_xGa_{1-x}As/GaAs$ quantum-well heterostructures due to carrier tunneling, Phys. Rev. B **31**, 7859 (1985).

[41] E. E. Mendez, G. Bastard, L. L. Chang, L. Esaki, H. Morkoc, and R. Fischer, Effect of an electric field on the luminescence of GaAs quantum wells, Phys. Rev. B **26**, 7101(R) (1982).

[42] C. Chen, X. Lu, B. Deng, X. Chen, Q. Guo, C. Li, C. Ma, S. Yuan, E. Sung, K. Watanabe, *et al.*, Widely tunable mid-infrared light emission in thin-film black phosphorus, Sci. Adv. **6**, eaay6134 (2020).

[43] N. Scheuschner, O. Ochedowski, A.-M. Kaulitz, R. Gillen, M. Schleberger, and J. Maultzsch, Photoluminescence of freestanding single- and few-layer MoS_2, Phys. Rev. B **89**, 125406 (2014).

[44] W. Zhao, R. M. Ribeiro, M. Toh, A. Carvalho, K. Kloc, A. H. Castro Neto, and G. Eda, Origin of indirect optical transitions in few-layer MoS_2, WS_2, and WSe_2, Nano Lett. **13**, 5627 (2013).

[45] K. F. Mak, C. Lee, J. Hone, J. Shan, and T. F. Heinz, Atomically thin MoS_2: A new direct-gap semiconductor, Phys. Rev. Lett. **105**, 136805 (2010).

[46] J. M. Hollas, *Modern Spectroscopy* (Wiley, Chichester, England, 2004), 4th ed.

[47] M. Romagnoli, V. Sorianello, M. Midrio, F. H. L. Koppens, C. Huyghebaert, D. Neumaier, P. Galli, W. Templ, A. D'Errico, and A. C. Ferrari, Graphene-based integrated photonics for next-generation datacom and telecom, Nat. Rev. Mater. **3**, 392 (2018).

[48] Z. P. Sun, A. Martinez, and F. Wang, Optical modulators with 2D layered materials, Nat. Photonics **10**, 227 (2016).

[49] D. Sun, Y. Zhang, D. Wang, W. Song, X. Liu, J. Pang, D. Geng, Y. Sang, and H. Liu, Microstructure and domain engineering of lithium niobate crystal films for integrated photonic applications, Light Sci. Appl. **9**, 197 (2020).

[50] K. Liu, C. R. Ye, S. Khan, and V. J. Sorger, Review and perspective on ultrafast wavelength-size electro-optic modulators, Laser Photonics Rev. **9**, 172 (2015).

[51] P. Iannone, X. Chen, S. Grillanda, G. Raybon, A. Adamiecki Burrows, T.-C. Hu, D. T. Neilson, N. Basavanhally, Y. Low, *et al.*, Pam-4 transmission up to 160 Gb/s with surface-normal electro-absorption modulators, Opt. Lett. **45**, 4484 (2020).

[52] H. Agarwal, B. Terrés, L. Orsini, A. Montanaro, V. Sorianello, M. Pantouvaki, K. Watanabe, T. Taniguchi, D. Van Thourhout, M. Romagnoli, *et al.*, 2d-3d integration of hexagonal boron nitride and a high-κ dielectric for ultrafast graphene-based electro-absorption modulators, Nat. Commun. **12**, 1070 (2021).

[53] T. Gu, H. J. Kim, C. Rivero-Baleine, and J. Hu, Reconfigurable metasurfaces towards commercial success, Nat. Photonics **17**, 48 (2023).

[54] S. Riyopoulos, Electrostatically shielded quantum confined stark effect inside polar nanostructures, Nanoscale Res. Lett. **4**, 993 (2009).

[55] M. M. Ugeda, A. J. Bradley, S.-F. Shi, F. H. da Jornada, Y. Zhang, D. Y. Qiu, W. Ruan, S.-K. Mo, Z. Hussain, Z.-X. Shen, *et al.*, Giant bandgap renormalization and excitonic effects in a monolayer transition metal dichalcogenide semiconductor, Nat. Mater. **13**, 1091 (2014).

[56] Y. Lin, X. Ling, L. Yu, S. Huang, A. L. Hsu, Y.-H. Lee, J. Kong, M. S. Dresselhaus, and T. Palacios, Dielectric screening of excitons and trions in single-layer MoS_2, Nano Lett. **14**, 5569 (2014).

[57] X. Hou, J. Kang, H. Qin, X. Chen, J. Ma, J. Zhou, L. Chen, L. Wang, L.-W. Wang, and X. Peng, Engineering auger recombination in colloidal quantum dots via dielectric screening, Nat. Commun. **10**, 1750 (2019).

[58] M. Florian, M. Hartmann, A. Steinhoff, J. Klein, A. W. Holleitner, J. J. Finley, T. O. Wehling, M. Kaniber, and C. Gies, The dielectric impact of layer distances on exciton and trion binding energies in van der Waals heterostructures, Nano Lett. **18**, 2725 (2018).

[59] K. F. Mak, K. He, C. Lee, G. H. Lee, J. Hone, T. F. Heinz, and J. Shan, Tightly bound trions in monolayer MoS_2, Nat Mater. **12**, 207 (2013).

[60] J. Pei, J. Yang, R. Xu, Y.-H. Zeng, Y. W. Myint, S. Zhang, J.-C. Zheng, Q. Qin, X. Wang, W. Jiang, *et al.*, Exciton and trion dynamics in bilayer MoS_2, Small **11**, 6384 (2015).

[61] G. Kresse and J. Furthmuller, Efficient iterative schemes for *ab initio* total-energy calculations using a plane-wave basis set, Phys. Rev. B **54**, 11169 (1996).

[62] P. E. Blochl, Projector augmented-wave method, Phys. Rev. B **50**, 17953 (1994).

[63] J. P. Perdew, K. Burke, and M. Ernzerhof, Generalized gradient approximation made simple, Phys. Rev. Lett. **77**, 3865 (1996).

[64] S. Grimme, S. Ehrlich, and L. Goerigk, Effect of the damping function in dispersion corrected density functional theory, J. Comput. Chem. **32**, 1456 (2011).

[65] S. Grimme, J. Antony, S. Ehrlich, and H. Krieg, A consistent and accurate *ab initio* parametrization of density functional dispersion correction (DFT-d) for the 94 elements H-Pu, J. Chem. Phys. **132**, 154104 (2010).

[66] K. Momma and F. Izumi, Vesta 3 for three-dimensional visualization of crystal, volumetric and morphology data, J. Appl. Crystallogr. **44**, 1272 (2011).

[67] VASP, Vasp wiki: Isym, Website (2013), https://www.vasp.at/wiki/index.php/ISYM.

[68] A. Kuc and T. Heine, The electronic structure calculations of two-dimensional transition-metal dichalcogenides in the presence of external electric and magnetic fields, Chem. Soc. Rev. **44**, 2603 (2015).

[69] X. Zhang, X.-F. Qiao, W. Shi, J.-B. Wu, D.-S. Jiang, and P.-H. Tan, Phonon and Raman scattering of two-dimensional transition metal dichalcogenides from monolayer, multilayer to bulk material, Chem. Soc. Rev. **44**, 2757 (2015).

[70] Q. Liu, L. Li, Y. Li, Z. Gao, Z. Chen, and J. Lu, Tuning electronic structure of bilayer MoS_2 by vertical electric field: A first-principles investigation, J. Phys. Chem. C **116**, 21556 (2012).